

Computer Modeling Wind Turbine Blades with Optimal Parameters

OLENA SIERIKOVA^{1,*}, ELENA STRELNIKOVA², KYRYL DEGTYAREV²

¹ Department of Environmental Protection Technologies,
National University of Civil Defence of Ukraine,
vul. Chernishevskya, 94, Kharkiv, 61023,
UKRAINE

²Department of Hydroaeromechanics of Power Machines,
Anatolii Pidhornyi Institute of Power Machines and Systems,
National Academy of Sciences of Ukraine
vul. Komunalnykiv, 2/10, Kharkiv, 61046,
UKRAINE

**Corresponding Author*

Abstract: - This paper aims to create efficient techniques to optimize the weight of wind turbine blades. A new mathematical model has been introduced, applying boundary element methods. Hypersingular integral equations have been used to calculate the dynamic pressure acting on the blade. The finite Hadamard part of the hypersingular integral has been received analytically over an arbitrary flat polygon. A revised version of the nonlinear programming method has been developed, which incorporates adaptive management techniques to optimize the procedures. The proposed optimization method uses several methods, called hybrids. A criterion has been specified by which the most effective hybrids are selected for the current search for an extremum. This criterion includes information characterizing a changing situation. The computer simulation results indicate that the wind turbine blade with the minimal weight has been achieved. Additionally, the proposed method will be extended to include the strength and dynamic analysis of wind turbines with a vertical axis of rotation.

Key-Words: - wind turbine blades, hypersingular integral equation, nonlinear programming, weight optimization, boundary element method, wind power plants, air pressure.

Received: July 27, 2024. Revised: December 7, 2024. Accepted: February 5, 2025. Published: March 7, 2025.

1 Introduction

Modern wind power plants are complex systems composed of numerous interconnected components with various functions. Among these, the windmill's vane system plays a central role. To optimally design structures of this type, search methods have been employed to identify the best set of parameters that meet the specified constraints and yield the most favorable outcome according to a chosen optimization criterion. While such methods are well-established, their effectiveness could vary depending on the changing conditions during the optimization process, and it is not always possible to achieve success within a reasonable time frame using any single method, [1]. The research presented introduces a novel hybrid optimization approach, which has been successfully applied to solve multi-parameter nonlinear programming

problems while considering both system constraints and functional limitations, [2].

Numerous numerical methods have been developed to assess the dynamic and strength characteristics of small wind turbines, [3], [4]. For the optimal design of both large and small turbines, two main types of computational techniques are typically employed: dynamic and strength analysis, along with nonlinear programming. For stress-strain analysis, methods such as finite element [5] and boundary element [6] methods, finite volume methods [7], and computational dynamics techniques [8], [9] have proven effective. Additionally, some advanced numerical methods, based on the immersion approach and focused on the strength and stability of aerospace structures, are also worth noting [10], alongside experimental studies [11].

The contemporary aspects of nonlinear programming have been discussed in [12]. An

effective numerical method for optimal design specifically applied to cyclically symmetrical structures, has been further developed in [13]. It is important to note that the numerical implementation of finite element and volume element methods, including turbulence models, demands significant computational time. This could create challenges when applying optimization procedures that require numerous evaluations of the objective function and constraints. As a result, boundary element methods [14] and other mesh-reduced approaches [15] are gaining prominence for optimal structural design.

In this paper, two effective numerical techniques have been applied. The first is a hypersingular integral method, implemented with boundary elements [16], to determine the dynamic characteristics of the blade. The second method has been based on nonlinear programming, [2]. By combining these approaches, new and efficient techniques for the optimal design of wind turbine blades have been developed, [17].

2 Problem Formulation

To compute the stress-strain state, the blade has been modeled as a thin-walled, naturally twisted rod with a variable cross-section and length LLL , fixed to the wind turbine hub, [18]. A coordinate system has been chosen where ZG represents the axis of rotation, and XG aligns with the axis of the wind wheel, as shown in Figure 1. The YG direction has been selected such that the global coordinate system is right-handed. For the stress-strain analysis of the blade, a local coordinate system (x,y,z) has been defined, with axes parallel to XG , YG , and ZG , respectively. The origin of this system has been placed at the center of gravity of the section.

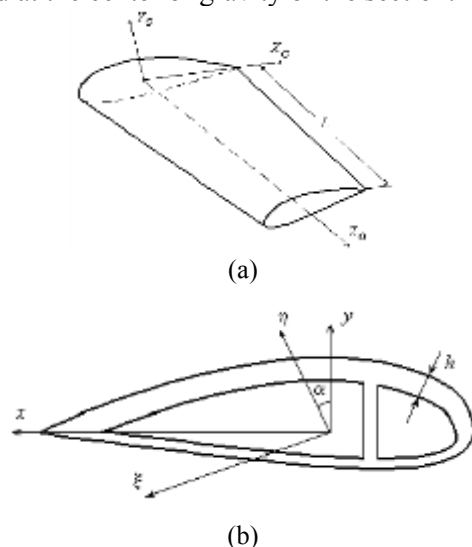


Fig. 1: Blade model a) and its section b)

The blade geometry has been described by a series of cross-sectional profiles. For each section, the following parameters have been specified: the coordinates (x,y) of the outer contour and the section thickness $h(z)$.

It has been assumed that the blade experiences aerodynamic loads and centrifugal forces. The calculated aerodynamic load has been reduced to distributed lateral forces \mathbf{q}_x , \mathbf{q}_y and distributed torque \mathbf{m}_z . For illustration, a blade with the following characteristics has been considered. The blade length, including the extension, is $L = 19.13$ m. The elastic constants are as follows: the modulus of elasticity of the extension $E_0 = 2 \cdot 10^5$ MPa, and the modulus of elasticity of the blade E varies from $4.92 \cdot 10^4$ up to $2.5 \cdot 10^4$ MPa; Poisson's ratio is $\nu = 0.18$, material density is $\rho = 1.6 \cdot 10^3$ kg/m³. The wind turbine rotation speed is $\Omega = 55$ rpm and the wind speed is 10 m/s. The number of blade sections is assumed to be 65. The thickness of the sections varies from 5 mm at the root to 2 mm at the tip, with the thickness of the extension section fixed at 8 mm. Displacements and stress distributions in the blade under aerodynamic and centrifugal loads have been estimated, [18].

The air environment has been assumed to be ideal, incompressible, and free of vortices. The problem of flow distribution around the blade could be reduced to solve a hypersingular integral equation, which allows for determining the pressure variation along the blade. The aeroelasticity problem has been addressed in an uncoupled formulation, meaning that the deformations and displacements of the blade are not assumed to affect the aerodynamic forces acting on it.

For the optimal design of such structures, procedures have been required to minimize (or maximize) an objective function by appropriately selecting design parameters within specified constraints. These constraints are also functions of the initial parameters.

The formulation of the optimization problem for the wind turbine blade has been described. The purpose is to find the blade with the minimum weight while satisfying the following conditions: under steady aerodynamic loads and centrifugal forces, the normal displacement w should not exceed a given value $[w]$, the stresses must be limited to $[\sigma]$, and the first natural frequency of vibration ω must also remain below a specified threshold.

Thus, for $i=1, \dots, N$ there are:

$$|\max w^i| \leq [w], |\max \sigma^i| \leq [\sigma], [\omega_1] \leq \quad (1)$$

$$\omega \leq [\omega_2].$$

The objective function here is the blade mass $m = \rho V$, where ρ is the material density, V is the blade volume defined as:

$$V = \sum_{i=1}^{N-1} \int_{z_i}^{z_{i+1}} S(z) dz, \quad (2)$$

where $S(z)$ is the cross-sectional area, $(N - 1)$ is section number.

The variable parameters in this case are the thicknesses of the blade at different sections $h_i(z)$, $i = 1, \dots, N$.

Thus, the extremal problem outlined in (1)-(2) is a nonlinear programming problem [2], [15], where the goal is to determine the vector

$$X^* = \arg \operatorname{extr}_{X \in G} F(X), \quad (3)$$

$$F(X) = \rho V$$

in the domain

$$G = \{X: G_i(X) \geq 0, i = \overline{1, m}\} \neq \emptyset \quad (4)$$

of the finite-dimensional parametric space E_n , which provides the extremum of the given objective function $F(X)$, defined within a certain extension $H \supset G$.

3 Problem Solution

3.1 Hypersingular Integral Equation Technique

To calculate aerodynamic loads, the blade has been represented by a finite-dimensional bearing surface, S_1 . Using the theory of bearing surfaces, various problems have been addressed and solved regarding the lift force on turbine blades [2], helicopter rotors [19], ship propellers [20], rotary-blade hydraulic turbine impellers [21], and wind wheel blades [4]. On this surface, a vortex layer originates from the trailing edge, taking the form of a vortex sheet, S_2 , that propagates in the direction of the incoming flow velocity, V_0 . In this context, the pressure drop ΔP across the blades has been determined using the Cauchy-Lagrange integral, which in this specific case is expressed as

$$\frac{\Delta P}{\rho_0} = -(\operatorname{grad} \gamma \cdot \mathbf{V}_R), \quad (5)$$

where ρ_0 is the liquid density, γ is the velocity circulation, \mathbf{V}_R is the relative fluid velocity, $\mathbf{V}_R = \mathbf{V}_0 - \boldsymbol{\Omega} \times \mathbf{r}$, and \mathbf{r} is the point radius-vector under consideration.

Consider the problem of an ideal incompressible fluid flowing around a thin load-bearing surface. Since the flow has been assumed to be irrotational

in all regions outside the bearing surface S_1 and the vortex wake S_2 behind it, there exists a potential function for the absolute fluid velocity. This potential satisfies the Laplace equation in the regions outside the discontinuity surfaces S_1 and S_2 .

$$\nabla^2 \Phi = 0. \quad (6)$$

Require that the non-flow condition be satisfied on the bearing surface S_1 ,

$$\frac{\partial \Phi^+}{\partial \mathbf{n}} = \frac{\partial \Phi^-}{\partial \mathbf{n}} = (\mathbf{V}_0, \mathbf{n}), \quad (7)$$

as well the absence of pressure's drop along the vortex wake S_2

$$(\operatorname{grad}(\Phi^+ - \Phi^-) \cdot \mathbf{V}_R) = 0. \quad (8)$$

Furthermore, it is necessary to satisfy the condition of attenuation of perturbed velocities at infinity:

$$\operatorname{grad} \Phi|_{\infty} = 0.$$

The most suitable representation for solving the above-described problem of the Laplace equation is through the use of a double-layer potential, [22]

$$\Phi(\mathbf{x}) = \frac{1}{4\pi} \iint_S \gamma(\boldsymbol{\xi}) \frac{\partial}{\partial \mathbf{n}_{\boldsymbol{\xi}}} \frac{1}{|\mathbf{x} - \boldsymbol{\xi}|} dS_{\boldsymbol{\xi}}. \quad (9)$$

Aerodynamic loads have been calculated by solving hypersingular integral equations using the boundary element method, as detailed in [23], [24]. The problem will be reduced to solve the following hypersingular equation.

$$\frac{1}{4\pi} \iint_S \gamma(\boldsymbol{\xi}) \frac{\partial^2}{\partial \mathbf{n}_{\mathbf{x}} \partial \mathbf{n}_{\boldsymbol{\xi}}} \left(\frac{1}{|\mathbf{x} - \boldsymbol{\xi}|} \right) dS_{\boldsymbol{\xi}} = g(\mathbf{x}), \quad (10)$$

$$g(\mathbf{x}) = (\mathbf{V}_0 \cdot \mathbf{n}(\mathbf{x})).$$

The vectors $\mathbf{n}_{\mathbf{x}}, \mathbf{n}_{\boldsymbol{\xi}}$ in equations (9) and (10) represent unit normals to the surface S at the points \mathbf{x} and $\boldsymbol{\xi}$, respectively. It is important to note that the integral in equation (10) is defined in the Hadamard sense, [24]. While this approach introduces significant computational challenges, the formulation in equation (10) satisfies the Laplace equation, the Sommerfeld condition, and ensures the continuity of the normal derivative (7) when crossing the surface S . Therefore, it is effective for analysing fluid-structure interaction problems where a liquid is in bilateral contact with the structure, in simulating the strength and dynamic properties of elements such as wind turbine blades, components of launch vehicles, and for various applications within hydroelasticity theory.

The finite part of the integral in (10) according to Hadamard at $\mathbf{x} \in S$ is the following limit, [25]:

$$I(\mathbf{x}) = \lim_{\varepsilon \rightarrow 0} \left[\frac{1}{4\pi} \iint_{S^*} \gamma(\boldsymbol{\xi}) \frac{\partial^2}{\partial \mathbf{n}_{\mathbf{x}} \partial \mathbf{n}_{\boldsymbol{\xi}}} \frac{1}{|\mathbf{x} - \boldsymbol{\xi}|} dS_{\boldsymbol{\xi}} - \right. \quad (11)$$

$$-\frac{\gamma(\mathbf{x})}{\varepsilon}] ,$$

where $S^* = S \setminus S^0$, and S^0 is a circle of radius ε , and with \mathbf{x} as center.

Calculate analytically the normal derivative of the double layer harmonic potential (10) in the sense of the Hadamard finite part, supposing that S is a flat polygon.

The following formula is in use:

$$I(\mathbf{x}) = \lim_{\varepsilon \rightarrow 0} I(\mathbf{x}') = \lim_{\varepsilon \rightarrow 0} \iint_S \gamma(\xi) \frac{\partial^2}{\partial n_x \partial n_\xi} \frac{1}{|\mathbf{x}' - \xi|} dS_\xi, \quad (12)$$

It has been assumed the point $\mathbf{x}' = \mathbf{x} + \varepsilon \mathbf{n}_x$ belongs the normal \mathbf{n}_x to the surface S in the point \mathbf{x} (the normal has been directed along the Oz axis). Denote by (x_i, y_i, z_i) ($i=1, 2, \dots, n$) coordinates of the vertices M_i of polygon S , and let $\mathbf{x} = (x_0, y_0, z_0)$, $\xi = (x, y, z)$. Since S is the flat domain, the integral in (12) just before the limiting value has been calculated by:

$$I(\mathbf{x}') = \gamma_0 \iint_S \left[-\frac{1}{r_1^3} + \frac{3\varepsilon^2}{r_1^5} \right] dS_y, \quad r_1 = \sqrt{(x - x_0)^2 + (y - y_0)^2 + \varepsilon^2}. \quad (13)$$

In the polar coordinate system $x - x_0 = \rho \cos \varphi$, $y - y_0 = \rho \sin \varphi$, and after some transformation, integral (13) became:

$$I(\mathbf{x}') = \gamma_0 \sum_{i=1}^n \int_{\varphi_i}^{\varphi_{i+1}} d\varphi \int_0^{\rho(\varphi)} \left[-\frac{1}{r_1^3} + \frac{3\varepsilon^2}{r_1^5} \right] \rho d\rho, \quad (14)$$

where

$$\begin{aligned} \varphi_i &= \arcsin \frac{y_i - y_0}{r_{i0}}, \quad r_{i0} = \\ &= \sqrt{(x_i - x_0)^2 + (y_i - y_0)^2 + \varepsilon^2}, \quad i = \\ &= 1, 2, \dots, n, \quad \varphi_{n+1} = \varphi_1, \\ \rho_i(\varphi) &= \frac{c_i}{\sin(\varphi - \varphi_i^*)}, \quad c_i = \\ &= \frac{[(y_i - y_0)(x_{i+1} - x_i) - (x_i - x_0)(y_{i+1} - y_i)]}{r_{i,i+1}}, \quad \varphi_i^* = \\ &= \arcsin \frac{y_{i+1} - y_i}{r_{i+1,i}}, \\ r_{i+1,i} &= \sqrt{(x_{i+1} - x_i)^2 + (y_{i+1} - y_i)^2 + \varepsilon^2}, \\ y_{n+1} &= y_1, \quad x_{n+1} = x_1. \end{aligned}$$

So, it has been obtained the following formula:

$$I(\mathbf{x}) = \gamma_0 \sum_{i=1}^n J_i(\mathbf{x}), \quad (15)$$

$$J_i(\mathbf{x}) = \int_{l_i} \left(\text{grad} \frac{1}{r} \times \mathbf{n} \right) \cdot d\mathbf{l}_i.$$

Here \mathbf{l}_i are the line segments connected vertices M_i and M_{i+1} of the considered polygon, $M_i = (x_i, y_i, z_i)$ and $M_{i+1} = (x_{i+1}, y_{i+1}, z_{i+1})$. The straight line equation \mathbf{l}_i in the parametric form could be written as:

$$\begin{aligned} x &= x_{i+1} + (x_{i+1} - x_i)t, \\ y &= y_{i+1} + (y_{i+1} - y_i)t, \\ z &= z_{i+1} + (z_{i+1} - z_i)t. \end{aligned}$$

The next vectors has been presented as:

$$\begin{aligned} \mathbf{l}_i &= (x_{i+1} - x_i, y_{i+1} - y_i, z_{i+1} - z_i), \\ \mathbf{r}_i &= (x_i - x_0, y_i - y_0, z_i - z_0), \\ \mathbf{n} &= (n_1, n_2, n_3). \end{aligned}$$

Then it will be obtained:

$$\begin{aligned} \left(\text{grad} \frac{1}{r} \times \mathbf{n} \right) \cdot d\mathbf{l}_i &= \\ &= \frac{1}{r^3} \begin{vmatrix} dx & dy & dz \\ x - x_0 & y - y_0 & z - z_0 \\ n_1 & n_2 & n_3 \end{vmatrix}, \end{aligned} \quad (16)$$

where

$$\begin{aligned} dx &= (x_{i+1} - x_i)dt, \quad dy = (y_{i+1} - y_i)dt, \\ dz &= (z_{i+1} - z_i)dt. \end{aligned}$$

After integrating over t from 0 to 1, the follow formula will be obtained:

$$J_i(\mathbf{x}) = \frac{[l_i \times \mathbf{r}_i] \cdot \mathbf{n}}{|[l_i \times \mathbf{r}_i]|^2} \left[\frac{[l_i \cdot \mathbf{r}_{i+1}]}{r_{i+1}} - \frac{[l_i \cdot \mathbf{r}_i]}{r_i} \right], \quad (17)$$

Here $r_i = |\mathbf{r}_i|$

Using formulas (15), (17), one could estimate the considered hypersingular integral over the flat polygon, arbitrarily oriented in space.

If the integration domain is a rectangular in the form $S = [-b < x < b, -l < y < l]$, then equation (18) takes the next simplified form:

$$\begin{aligned} I(\mathbf{x}) &= \gamma_0 L(\mathbf{x}), \quad (18) \\ L(\mathbf{x}) &= \left[-\frac{\sqrt{(x-b)^2 + (y-l)^2}}{(x-b)(y-l)} + \right. \\ &+ \frac{\sqrt{(x-b)^2 + (y+l)^2}}{(x-b)(y+l)} + \\ &+ \left. \frac{\sqrt{(x+b)^2 + (y-l)^2}}{(x+b)(y-l)} - \frac{\sqrt{(x+b)^2 + (y+l)^2}}{(x+b)(y+l)} \right]. \end{aligned}$$

The computational domain has been discretized by N_S boundary elements as:

$$S = \bigcup_{k=1}^{N_S} S_k, \quad (19)$$

where S_k are flat polygons. The unknown density will be denoted as $\gamma(\xi)$ is a constant over each boundary element S_k and denoted by γ_k . Let \mathbf{x}_{0j} , $j = 1, 2, \dots, N_S$ be the collocation points. These points are selected as the centroids of the boundary elements. The hypersingular integrals over the boundary elements are computed using the formulas (15)-(17). The following system of linear algebraic equations has been gained

$$\sum_{k=1}^{N_S} H_{kj} \gamma_k = f(\mathbf{x}_{0j}), \quad j = 1, 2, \dots, N_S, \quad (20)$$

to determine the discrete values γ_k of the unknown density $\gamma(\boldsymbol{\xi})$. Here:

$$H_{kj} = \frac{1}{4\pi} \iint_{S_k} \frac{\partial^2}{\partial \mathbf{n}_x \partial \mathbf{n}_\xi} \frac{1}{|\mathbf{x}_{0j} - \boldsymbol{\xi}|} dS_k, \cdot \gamma_k = \gamma(\mathbf{x}_{0k}).$$

So, the discrete analogue is obtained for hypersingular integral equation (10), i. e. hypersingular integral equation (10) has been solved due to reducing to the f system of linear algebraic equations (20).

3.2 Application to Fluid-Structure Interaction Problems

Hypersingular integral equations (HIE) are highly effective for solving fluid-structure interaction problems, particularly when structural elements are in bilateral contact with liquids. This approach significantly reduces the dimensionality of the resulting systems of linear algebraic equations. Additionally, applying HIE enables direct solutions for the desired unknown functions without requiring further complex calculations

In this paper fluid-structure interactions involving structural elements submerged in liquid is examined. This study applies the normal mode method [26], in this approach, the vibration mode of a structural element interacting with a fluid has been expressed as a linear combination of the element's natural modes in vacuo (i.e., without the influence of the surrounding fluid mass). One of the main advantages of this method is that the natural vibration modes in vacuo could be determined using various techniques, such as analytical solutions or the boundary and finite element methods. While analytical solutions are typically only feasible for structural elements with simple geometries, the finite element method necessitates discretizing the entire fluid domain, which results in significantly higher computational costs compared to boundary element methods. The vibrations of the deformable element within the fluid are governed by a system of differential equations, [22]

$$\mathbf{M}\ddot{\mathbf{U}} + \mathbf{K}\mathbf{U} = \mathbf{f}_{pr} + \mathbf{f}_s, \quad (21)$$

where \mathbf{M} and \mathbf{K} have been designated the mass and stiffness matrices, respectively, \mathbf{f}_{pr} is the vector characterizing the fluid pressure overfall, and \mathbf{f}_s is an external forces vector.

The pressure overfall \mathbf{f}_{pr} over S has been calculated by the follow formula:

$$\mathbf{f}_{pr} = -\rho_0 \frac{\partial}{\partial t} [\varphi^+(\mathbf{x}, t) - \varphi^-(\mathbf{x}, t)] \mathbf{n},$$

where ρ_0 is the liquid density, φ is the velocity potential, and \mathbf{n} is the unit positive normal to the surface S .

To determine the unknown potential φ , the next boundary value problem for Laplace's equation has been formulated:

$$\Delta\varphi = 0, \quad \frac{\partial\varphi(\mathbf{x})}{\partial \mathbf{n}^\pm} = \left(\frac{\partial \mathbf{U}}{\partial t}, \mathbf{n} \right), \quad \text{grad}\varphi|_\infty = 0. \quad (22)$$

According to [26] there will be gained:

$$\mathbf{U}(\mathbf{x}, t) = \sum_{k=1}^N c_k(t) \mathbf{u}_k(\mathbf{x}),$$

where $c_k(t)$ are the unknown time-dependent coefficients, and $\mathbf{u}_k(\mathbf{x})$ are the structural element vibration modes of the in vacuo. These functions were calculated using the finite element method as in [4]. Then the unknown potential has been expressed as

$$\varphi(\mathbf{x}, t) = \sum_{k=1}^N \dot{c}_k(t) \varphi_k(\mathbf{x}).$$

For the participial potentials $\varphi_k(\mathbf{x})$ the following boundary value problems have been formulated:

$$\Delta\varphi_k = 0, \quad \frac{\partial\varphi_k(\mathbf{x})}{\partial \mathbf{n}^\pm} = (\mathbf{u}_k, \mathbf{n}), \quad \text{grad}\varphi_k|_\infty = 0 \quad (23)$$

After receiving the basis functions \mathbf{u}_k and φ_k , one could obtain the following relations:

$$\sum_{k=1}^N [\dot{c}_k(t) \mathbf{M}\mathbf{u}_k + c_k(t) \mathbf{K}\mathbf{u}_k] = -\rho_l \sum_{k=1}^N \dot{c}_k(t) [\varphi_k^+(\mathbf{x}) - \varphi_k^-(\mathbf{x})] \mathbf{n} + \mathbf{f}_s. \quad (24)$$

To define φ_k the boundary element method is in use [27], so the solution of boundary value problem (23) for each k is the double layer potential along the surface S with the unknown density $\gamma_k(\boldsymbol{\xi})$

$$\varphi_k(\mathbf{x}) = \frac{1}{4\pi} \iint_S \gamma_k(\boldsymbol{\xi}) \frac{\partial}{\partial \mathbf{n}_\xi} \frac{1}{|\mathbf{x} - \boldsymbol{\xi}|} dS,$$

Note that $\varphi_k(\mathbf{x})$ satisfies Laplace's equation and Sommerfeld's condition, and

$$\gamma_k(\mathbf{x}) = \varphi_k^+(\mathbf{x}) - \varphi_k^-(\mathbf{x}).$$

To evaluate $\gamma_k(\mathbf{x})$ the hypersingular integral equation (10) with the right parts in the form $(\mathbf{u}_k, \mathbf{n})$ has been applied. Then according the equation (24) dot product sequentially with the functions $\mathbf{u}_l(\mathbf{x})$ the next second order system of differential equations has been obtained:

$$\mathbf{M}_s[\ddot{\mathbf{c}}] + \mathbf{M}_l[\dot{\mathbf{c}}] + \mathbf{K}_s[\mathbf{c}] = \tilde{\mathbf{f}}_s, \quad (25)$$

where

$$\mathbf{M}_s = (\mathbf{M}\mathbf{u}_k, \mathbf{u}_l), \mathbf{K}_s = (\mathbf{K}\mathbf{u}_k, \mathbf{u}_l), \tilde{\mathbf{f}}_s = (\mathbf{f}_s, \mathbf{u}_l).$$

The added masses matrix $\mathbf{M}_l = \{M_{l(i,k)}\}$ has been determined as:

$$M_{l(i,k)} = \rho_0 \iint_S \gamma_i(\mathbf{x}) w_k(\mathbf{x}) dS. \quad (26)$$

After determining M_l and supposing:

$$c_k(t) = \exp(i\omega t) \text{ with } \dot{f}_s = 0,$$

the eigenvalue problem

$$[\mathbf{K}_s - \omega^2(\mathbf{M}_s + \mathbf{M}_l)]\mathbf{W} = 0 \quad (27)$$

Has been solved using the method developed in [28].

3.3 Benchmark Test

To validate the method and determine the necessary number of boundary and finite elements, a test case from [29] is used, which compares theoretical results from various authors [29], [30] with experimental data [31]. As detailed in [29], the test involves a square elastic cantilever plate with the following mechanical and geometric properties: side length $a=10$ m, thickness $h=0.238$ m, Young's modulus $E=2.06$ GPa, Poisson's ratio $\nu=0.3$, material density ρ_s is 7830kg/m^3 , and liquid density ρ_0 is 1000kg/m^3 . The plate is submerged in water, as shown on Figure 2.

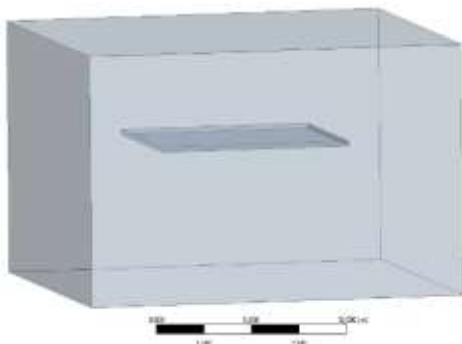
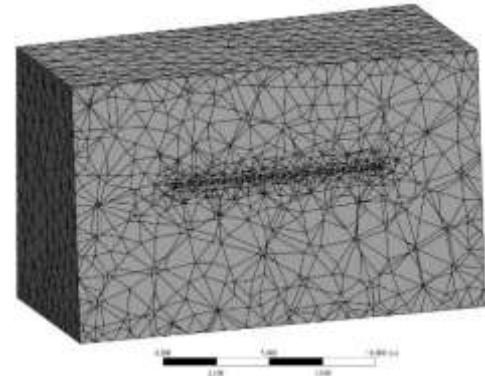


Fig. 2: The plate immersed in water

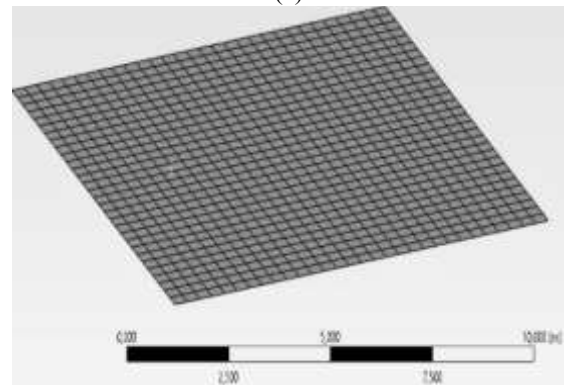
In the FEM calculation, the liquid domain is modeled as a parallelepiped with dimensions of 30 m by 30 m by 14 m, where 6 m lies above the plate and 78m below it. The finite element mesh for the plate contains 4,700 elements, Figure 3, while the liquid The grid is refined near the plate to enhance accuracy in capturing the fluid-structure interactions. In the FEM model, this thickened mesh provides more detailed resolution in the regions close to the plate surface, improving the calculation precision in these critical areasdomain is discretized into 38,500 elements, Figure 3(a).

One key advantage to use the Boundary Element Method (BEM) is that only the boundary of the computational domain needs to be discretized. In this case, the boundary consists solely of the elastic plate, as it has been assumed to be immersed in an infinite liquid domain. The Sommerfeld radiation condition at infinity has been inherently satisfied by

the characteristics of the double-layer potential. As a result, the boundary element mesh for the computational domain has been reduced to just 970 elements, as shown in Figure 3(b).



(a)



(b)

Fig. 3: Finite and boundary element grids

Initially, the modes and frequencies of the plate in a vacuum have been determined using FEM, [5]. These computed modes have been applied as input data to solve the hypersingular integral equation (10) with the right parts in the form $(\mathbf{u}_k, \mathbf{n})$ and, in turn, to derive the added mass matrix (26).

Table 1 presents the calculated frequencies of the plate both in a vacuum and submerged in water, applying several numerical techniques, such as the finite and boundary element methods, alongside a comparison with experimental data, [31].

Table 1. Frequencies of cantilever square plate immersed in water. Results comparison

Mode number	In vacuo			In water			
	[29]	[30]	Present method, FEM	[29]	[30]	Present method BEM	Experiment [31]
1	12.93	12.94	12.94	7.00	7.35	7.35	6.56
2	31.69	31.93	32.09	17.16	20.19	21.06	19.66
3	79.37	79.80	77.92	42.98	50.11	47.54	45.20

Test calculations provide an estimate of the required number of finite and boundary elements needed to achieve the desired accuracy and

demonstrate the effective application of the HIE technique in fluid-structure interaction problems.

3.4 Estimation of Aerodynamic Loads

After numerical solution of system (20), we obtain the unknown function $\gamma(\mathbf{x}_{0j})$ in the collocation points $\mathbf{x}_{0j} = (x_{0j}, y_{0j})$. Then the pressure drop ΔP has been gained using formula (5), where $\text{grad } \gamma$ has been calculated using finite difference formulas, namely:

$$\text{grad } \gamma(\mathbf{x}) = \left(\frac{\partial \gamma}{\partial x}, \frac{\partial \gamma}{\partial y} \right),$$

$$\frac{\partial \gamma(\mathbf{x}_{0j})}{\partial x} = \frac{\gamma(x_{0j+1}, y_{0j}) - \gamma(x_{0j}, y_{0j})}{x_{0j+1} - x_{0j}},$$

$$\frac{\partial \gamma(\mathbf{x}_{0j})}{\partial y} = \frac{\gamma(x_{0j}, y_{0j+1}) - \gamma(x_{0j}, y_{0j})}{y_{0j+1} - y_{0j}}.$$

Then with the known function ΔP , the distributed loads \mathbf{q}_x , \mathbf{q}_y and torque \mathbf{m}_z have been evaluated by the following formulas:

$$\mathbf{q}_x = q_x \mathbf{i}, \mathbf{q}_y = q_y \mathbf{j}, q_x = \Delta P \cos(\alpha_x), q_y = \Delta P \cos(\alpha_y), \mathbf{m}_z = \Delta P (\mathbf{n} \times \mathbf{r}). \quad (28)$$

In the numerical implementation of system (20), the numbers of integration subdomains have been assumed to be equal to $N_S = 100 \times 100$. In each subdomain, hypersingular integrals have been evaluated analytically using formulas (18). Increasing the values of N_{S2} did not lead to a significant change in the results. In Figure 4(a) and Figure 4(b) graphs of the lateral loads distribution and torque along the length of the blade have been shown.

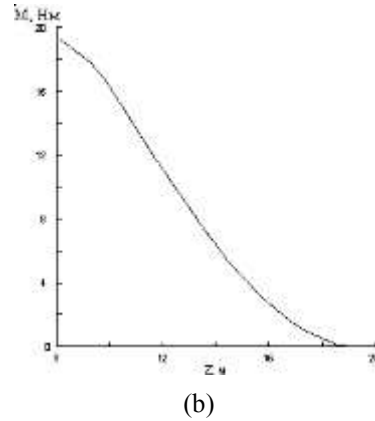
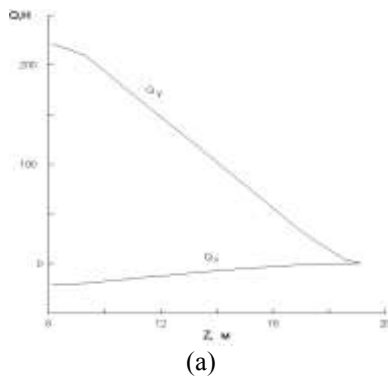


Fig. 4: Lateral load and torque distributions

The maximum displacement u in the plane of rotation of the wind wheel, normal to the OZ axis, is 160.9 cm. The maximum bending stresses arise in the cylindrical part of the extension and reach 290.8 MPa, in the root section of the blade, the stress is 73.8 MPa.

Stress distributions over the blade cross section and along the blade axis have been demonstrated on Figure 5(a) and Figure 5(b).

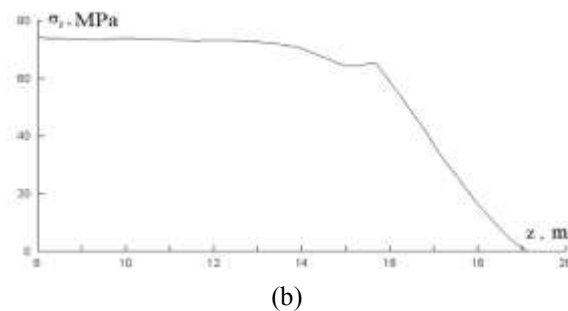
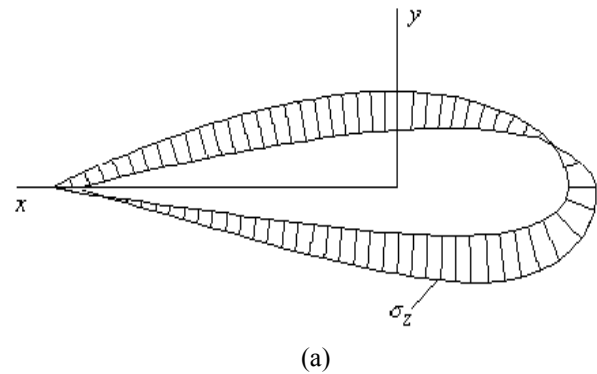


Fig. 5: Stress distribution

It is important to note that the stresses σ_z remain nearly constant over most of the blade, as shown in Figure 3(b). This outcome is due to the variation in the cross-sectional parameters along the length of the blade.

After evaluating the aerodynamic loads, the stress-strained state of the blade as well as free

vibration frequencies have been determined according to [32].

Displacements of the cross section have been represented as translational movements of the bending center and rotation of the section, relative to the bending center

$$U = u - \theta(y - y_u), V = v + \theta(x - x_u), \quad (29)$$

$$W = w - u'x - v'y + \theta'\phi,$$

where U, V, W are displacements of an arbitrary section point with (x, y, z) coordinates, u, v, w are displacements of the center of the section gravity, θ is an angular displacement around the bending center, x_u, y_u are coordinates of the bending center, ϕ is the deflection function, and $()' = d()/dz$.

The deformation' values at an arbitrary point (x, y, z) when using the kinematic model (29) have been expressed as follows

$$\begin{aligned} \varepsilon_z &= w' - u''x - v''y + \theta''\phi + \\ \theta'\tau_0 \left[\frac{\partial\phi}{\partial\xi}(\eta - \eta_u) - \frac{\partial\phi}{\partial\eta}(\xi - \xi_u) \right], \quad \varepsilon_x &= \varepsilon_y = \quad (30) \\ \varepsilon_{xy} &= 0, \\ \gamma_{xz} &= \theta' \left[\frac{\partial\phi}{\partial\xi} \cos \alpha - \frac{\partial\phi}{\partial\eta} \sin \alpha - (y - y_u) \right], \\ \gamma_{yz} &= \theta' \left[\frac{\partial\phi}{\partial\eta} \sin \alpha + \frac{\partial\phi}{\partial\xi} \cos \alpha + (x - x_u) \right], \end{aligned}$$

where ξ, η are main central axes of the section, $\alpha(z)$ is the twist angle, $\tau_0 = \alpha'$.

The potential energy of the blade deformation has been expressed by the integral

$$\Pi = \frac{1}{2} \int_0^L \int_{S(z)} [E\varepsilon_z^2 + G(\gamma_{xz}^2 + \gamma_{yz}^2)] dS(z) dz, \quad (31)$$

where E and G are the elastic moduli of the material in tension and shear.

The work of centrifugal forces A_C has been determined by the expression

$$A_C = \rho\Omega^2 \int_0^L [\theta J_{xy} + w(R+z)S(z)] dz, \quad (32)$$

where R is wind wheel radius, and

$$J_{xy} = \int_S xy dS.$$

The variational equation of elastic equilibrium has been obtained based on Lagrange's principle of possible displacements

$$\delta\Pi - \delta A_C - \delta A = 0, \quad (33)$$

here A is the work of distributed aerodynamic loads. In the numerical implementation, the finite element method [32] has been used to solve problem (33), a two-node element with cubic approximation of normal displacements u, v and linear approximation of axial displacement w is used. In this research 96 finite elements have been used for elastic analysis.

3.5 Hybrid Optimization Method with Adaptive Control

For the optimal design of complex multi-parameter objects of the considered type, it is useful to apply an automatic hybrid search optimization method [1] to determine the local optimal vector X^* for the conditional extremum problem, specifically in the context of problems (1)-(4).

An analysis of optimization procedures and the characteristics of solving optimal design problems reveals that simply accumulating effective methods in a software library, or even incorporating an interactive solution mode, does not create the necessary conditions for effective optimization. This is because the given problem does not come pre-equipped with the relevant set of attributes that would allow the control metaprogram to identify the situation and select the appropriate method.

The proposed method essence is as follows. There are a number of hybrid methods that make up the hybrid coalition $\{M_i\}$. The criterion $Q(\sigma)$ has been set, which determines during the process, which of the hybrids in given situation σ could be used to achieve the goal most effectively. This criterion includes information characterizing the changing situation σ ; namely, specificity of the structure and metric parameters of the space, where the search has been carried out, prehistory of the computing process by which a possible continuation has been established as well as behavior of the functions that determine the problem to solve. The control function $u = u(Q(\sigma))$ has been introduced, which establishes an adaptive strategy to put into operation a specific hybrid $M_k \in \{M_i\}, i = 1, \dots, k, \dots, s$ (or a group of methods-hybrids). The joint actions of methods-hybrids ensure a more effective achievement of the aim than each of the coalition individually hybrids. This could be achieved by introducing special adaptive control, which obtains vectors of minimizing sequences $\{X_{kr}\}$, search directions $\text{Dir } X_{kr}$, and search adaptive steps h_{kr} , in accordance with the changing situation σ .

In general, adaptive control u could be represented as

$$\begin{aligned} \left\{ \begin{array}{l} X_k^r \\ \text{Dir } X_k^r \\ h_k^r \end{array} \right\} &= \sum_{i=1}^s u_i(Q(\sigma_k)) \left\{ \begin{array}{l} X_k^{M_i} \\ \text{Dir } X_k^{M_i} \\ h_{ki} \end{array} \right\}, \quad (34) \\ \sum_{i=1}^s u_i(Q(\sigma_k)) &= 1, \end{aligned}$$

where $u_i(Q(\sigma_k))$ are non-negative control functions defined on the set $\{\sigma_k\}$ of situations, X_k^r , $\text{Dir } X_k^r$, and h_k^r are the point, the direction emanating from this point, and the adapting search step generated by M_i

method from the coalition $\{M_i\}$, respectively, k is the iteration number.

The hybridization operation or obtaining the hybrid point at the k^{th} step of the process could be defined as the following matrix-vector product:

$$X_k^r = \left(U_j^{(i)} \right) \left(X_j^{(i)} V(r) \right), \sum_{i=1}^N U_j^{(i)} = \quad (35)$$

$$\frac{\sum_{j=k-r+1}^N V_j(r)}{k-r+1, k, \quad k \geq r,$$

where $\left(U_j^{(i)} \right)$ and $\left(X_j^{(i)} \right)$ are matrices (of dimensions $(r \times N)$) of control and state, the elements of which are controls $U_j^{(i)}$ (scalars) and approximations $X_j^{(i)}$ (vectors of dimension n) of hybridents at a given step j , $V_j(r)$ is r -dimensional "compression" vector with scalar components, r is the memory depth of hybrids, and N is their number. The special product of scalar $\left(U_j^{(i)} \right)$ and vector matrices $\left(X_j^{(i)} \right)$ gives the vector Z , which components are vectors in the form

$$Z_j = \sum_{i=1}^m U_j^{(i)} X_j^{(i)}, \quad (36)$$

$$j = \overline{k-r+1, k}, \quad k \geq r$$

The following method modifications have been chosen as hybrids M_i for this version of the hybrid optimization method: adaptive step-by-step descent, Abramov scheme, ravine modification, the pattern recognition algorithm [33], Hooke-Jeeves, Davidon-Fletcher-Powell methods, parallel tangent method, secant motion along the boundary of region G , [15].

On the each selected search directions, one-dimensional minimization of the aim function has been carried out according, [12]. In [2] it has been presented the hybrid method could solve a wide class of problems much more efficiently than each of the abovementioned hybrids.

4 Results and Discussion

To gain the optimal design, the wind turbine blade with the following parameters has been investigated: $L=4$ m, elastic modulus $E=5 \cdot 10^5$ MPa, Poisson's ratio $\nu=0.3$, material density $\rho=1.6 \cdot 10^3$ kg/m³, wind wheel rotation speed $\Omega = 20$ rpm, wind speed 10m/s, $[\sigma]=200$ MPa, frequency range $[\omega_1] = 0.1$ Hz, $[\omega_2]=10$ Hz. The blade width varied from 1 m to 0.6 m.

In the problem solving process, the fields of displacements and stresses in the blade under

aerodynamic loads have been clarified. The section number has been chosen equal to 28.

The maximum displacement in the plane of the wind wheel rotation, normal to the OZ axis, is 28.5 cm, maximum bending stresses in the root section of the blade is 12.8 MPa, and the first frequency of natural oscillations is equal to 2.28 Hz. Table 2 presents the solution results of optimization problem for the blade sections Z_i series. The initial values of thickness in sections h_0 and optimal parameters h^* have been shown. In the initial version, the mass of the blade was equal to 19.38 kg.

As a optimization result, the blade with 16.64kg weight has been gained. The only active restriction was the blade displacement. The natural oscillation frequency has been changed slightly during the counting process, this change did not violate the specified restrictions. Thus, methods to calculate aerodynamic loads and analyze the stress-strain state of the wind turbine blades highlighted high efficiency and accuracy, which made it possible to formulate and solve optimization problems that require repeated verification calculations. Using the developed in-house hybrid adaptive method, the problem of weight optimization of wind turbine blades has been solved.

Table 2. Initial and Optimal Blade Parameters

Section Number	Coordinate z, m	Initial Thickness, mm	Optimal Thickness, mm
1	0.800	6.0	5.04
2	1.236	5.6	4.73
3	1.818	5.0	4.21
4	2.400	4.4	3.67
5	2.836	4.0	3.25
6	3.564	3.2	2.41
7	4.000	3.0	2.19

5 Conclusion and Further Research

An effective method for weight optimization of wind turbine blades has been proposed.

The mathematical model has been simulated to identify the air pressure on the wind turbine blade based on the hypersingular integral equations method, namely the boundary element method for its numerical application. In this study, a new version of a method to solve nonlinear programming problems has been developed, which combines several optimization techniques through adaptive control. It has been assumed that the unknown densities remain constant along the elements. The adaptive hybrid method of nonlinear programming has been applied to optimize the weight of the blade.

The blade of wind turbines has been evaluated, which enabled a reduction in its weight while still adhering to design and strength requirements. A major advantage in the practical application of the new blade design could be the blades' extension service life and the impact on the environmental minimization of wind power plants in the event of their premature destruction under wind loads and precipitation.

The further research in the area will be concerned with implementation of innovative composite materials for wind turbine blades producing, [34]. It allows to improve turbine blades mechanical characteristics. The proposed approach will be also generalized to strength and dynamical analysis of wind turbines with a vertical axis of rotation [35] as well as their weight optimization.

Acknowledgements:

The authors are very grateful to our foreign collaborators, professors Alexander Cheng, Wessex Institute of Technology, UK, and Jure Ravnik, Head of transport phenomena in fluid and solids laboratory, Maribor University, Slovenia, for their continued support and cooperation.

Declaration of Generative AI and AI-assisted Technologies in the Writing Process

During the preparation of this work the authors used chatgpt for language editing. After using this service, the authors reviewed and edited the content as needed and take full responsibility for the content of the publication.

References:

- [1] Smetankina N., Semenets O., Merkulova A., Merkulov D., Misura S., 2023. Two-Stage Optimization of Laminated Composite Elements with Minimal Mass. In: Arsenyeva, O., Romanova, T., Sukhonos, M., Tsegelnyk, Y. (eds) Smart Technologies in Urban Engineering. STUE 2022. *Lecture Notes in Networks and Systems*. Springer, Cham. vol 536: 456-465. https://doi.org/10.1007/978-3-031-20141-7_42.
- [2] Yershov S., Rusanov A., Shapochka A., Lampart P., Wirydczuk J., Gardzilewicz A., 2002. A Shape optimization of two turbine stages using the deformed polyhedron method and a three-dimensional RANS solver. *Proceedings of the Institution of Mechanical Engineers, Part A: Journal of Power and Energy*, 216(2): 203–213. <https://doi.org/10.3390/designs4030019>.
- [3] Battisti L., Benini E., Brighenti A., Dell'Anna S., Castelli M.R., 2018. Small wind turbine effectiveness in the urban environment. *Renew. Energy*, vol. 129: 102–113. <https://doi.org/10.1016/j.renene.2018.05.062>.
- [4] Sierikova O., Strelnikova E., Degtyariv K., 2023. Numerical Simulation of Strength and Aerodynamic Characteristics of Small Wind Turbine Blades. In: Nechyporuk, M., Pavlikov, V., Kritskiy, D. (eds) *Integrated Computer Technologies in Mechanical Engineering - 2022. ICTM 2022. Lecture Notes in Networks and Systems*. Springer, Cham. 657: 357-370. https://doi.org/10.1007/978-3-031-36201-9_31.
- [5] Kolodiazhna L., Bykov Y., 2023. Aeroelastic Characteristics of Rotor Blades of Last Stage of a Powerful Steam Turbine. *J. of Mech. Eng.*, vol. 26, no. 1: 6-14. <https://doi.org/10.15407/pmach2023.01.006>.
- [6] Sierikova O., 2024. *The Fundamentals of Boundary Element Methods*. NY: Nova Science Publishers, Inc. 150 p. <https://doi.org/10.52305/KFFP5657>.
- [7] Lampart P., Yershov S., Rusanov A., Szymaniak M., 2004. Tip leakage / main flow interactions in multi-stage HP turbines with short-height blading. *Proceedings of the ASME Turbo Expo 2004*, vol. 5: 1359-1367. <https://doi.org/10.1115/GT2004-53882>.
- [8] Yusof S. N. A., Asako Y., Sidik N. A. C., Mohamed S. B., Mohd W., Japar A. A., 2020. *A Short Review on RANS Turbulence Models*. *CFD Letters*, vol. 12(11): 83-96. <https://doi.org/10.37934/cfdl.12.11.8396>.
- [9] Mastrodicasa D., Di Lorenzo E., Manzato S., Guillaume P., 2022. Full-Field Modal Analysis by Using Digital Image Correlation Technique. *Rotating Machinery, Optical Methods & Scanning LDV Methods*, vol. 6, T
- [10] Umbricht G.F., Rubio D., Optimal Estimation of Thermal Diffusivity in a Thermal Energy Transfer Problem with Heat Generation, Convection Dissipation and Lateral Heat Flow, 2021. *WSEAS Transactions on fluid mechanics*, Vol.16, 232-238, <https://doi.org/10.37394/232013.2021.16.21>.
- [11] Rusanov A., Rusanov R., Klonowicz P., Lampart P., Żywica G., Borsukiewicz A., 2021. Development and experimental validation of real fluid models for CFD calculation of ORC and steam turbine flows.

- Materials*, 14(22): 6879.
<https://doi.org/10.3390/ma14226879>.
- [12] Sheludko G., Ugrimov S., 2016. The localization method of extremum points for unimodal function. *Journal of Mechanical Engineering*, Vol. 19, no. 1: 43-54.
<https://doi.org/10.15407/pmach2016.01.044>.
- [13] Misura S., Smetankina N., Misiura I., 2021. Optimal design of the cyclically symmetrical structure under static load. In: Nechyporuk, M., Pavlikov, V., Kritskiy, D. (eds.) *ICTM 2020. LNNS*, Vol. 188: 256–266. Springer, Cham, https://doi.org/10.1007/978-3-030-66717-7_21.
- [14] Liu H., Wang F., Qiu L., Chi C., 2024. Acoustic simulation using singular boundary method based on loop subdivision surfaces: A seamless integration of CAD and CAE. *Engineering Analysis with Boundary Elements*, Vol. 158: 97-106.
<https://doi.org/10.1016/j.enganabound.2023.10.022>.
- [15] Eisa S. A., 2019. Nonlinear Modeling, Analysis and Simulation of Wind Turbine Control System with and without Pitch Control as in Industry. *Advanced Control and Optimization Paradigms for Wind Energy Systems, Power Systems*, Publisher: Springer, Singapore: 1-40. https://doi.org/10.1007/978-981-13-5995-8_1.
- [16] Gnitko V., Karaiev A., Degtyariov K., Vierushkin I., Strelnikova E., 2022. Singular and hypersingular integral equations in fluid–structure interaction analysis. *WIT Transactions on Engineering Sciences*, Vol. 34: 67-79, <https://doi.org/10.2495/BE450061>.
- [17] Rzadkowski R., Gnesin V., Kolodyazhnaya L., 2018. Aeroelasticity Analysis of Unsteady Rotor Blade Forces and Displacements in LP Last Stage Steam Turbine with Various Pressure Distributions the Stage Exit. *J. Vib. Eng. Technol.* vol. 6: 333–337.
<https://doi.org/10.1007/s42417-018-0049-9>.
- [18] Mahmuddin F., 2017. Rotor Blade Performance Analysis with Blade Element Momentum Theory. *Energy Procedia*, Vol. 105: 1123–1129.
<https://doi.org/10.1016/j.egypro.2017.03.477>.
- [19] Pourmostafa M., Ghadimi P., 2020. Applying boundary element method to simulate a high-skew Controllable Pitch Propeller with different hub diameters for preliminary design purposes. *Cogent Engineering*, Vol. 7, no.1, V.: 1805857.
<https://doi.org/10.1080/23311916.2020.1805857>.
- [20] Kurennov S., Smetankina N., Pavlikov V., Dvoretzkaya D., Radchenko V., 2022. Mathematical Model of the Stress State of the Antenna Radome Joint with the Load-Bearing Edging of the Skin Cutout, In: Ciobotă D.D. (eds) International Conference on Reliable Systems Engineering (ICoRSE) - 2021. ICoRSE 2021. *Lecture Notes in Networks and Systems, Springer, Cham.* vol 305: 287-295.
https://doi.org/10.1007/978-3-030-83368-8_28.
- [21] Rusanov A., Chugay M., Rusanov R., 2023. Advanced Computer Technologies in the New Flow Part Development for Reactive Type HPC Steam Turbine of T-100 Series. In: Altenbach, H. Advances in Mechanical and Power Engineering. CAMPE 2021. *Lecture Notes in Mechanical Engineering. Springer, Cham.* https://doi.org/10.1007/978-3-031-18487-1_6.
- [22] Sierikova O., Strelnikova E., Kriutchenko D., Gnitko V., 2022. Reducing Environmental Hazards of Prismatic Storage Tanks under Vibrations, *WSEAS Transactions on Circuits and Systems*, Vol. 21: 249-257,
<https://doi.org/10.37394/23201.2022.21.27>.
- [23] Zang Q. S., Liu J., Zhang B., Qin L., Ye W. B., & Bordas S. 2024. Semi-analytical analysis of nonlinear liquid sloshing in rectangular tanks with scaled boundary finite element method. *Physics of Fluids*, Vol. 36(7): 075160.
<https://doi.org/10.1063/5.0213683>.
- [24] Grapow F., Raszewska D., Skalski R., Czarnecki J., Telega K., Miller M., Rogowski P., Prociów M. 2018. Small wind, big potential: HAWT design case study. MATEC Web of Conferences, vol. 234, 0100. DOI: 10.1051/mateconf/201823401005.
- [25] Obaiys S. J., Ibrahim R. W., Ahmad A. F., 2019. Hypersingular Integrals in Integral Equations and Inequalities: Fundamental Review Study. In: Andrica, D., Rassias, T. (eds) Differential and Integral Inequalities. *Springer Optimization and Its Applications. Springer, Cham.* Vol. 151.
https://doi.org/10.1007/978-3-030-27407-8_25.
- [26] Fu, Y. Price, W. G. 1987. Interactions between a partially or totally immersed vibrating cantilever plate and the surrounding fluid, *J. Sound Vibr.* Vol. 118(3): 495–513,

- [https://doi.org/10.1016/0022-460X\(87\)90366-X](https://doi.org/10.1016/0022-460X(87)90366-X).
- [27] Brebbia C.A., 2017. The birth of the boundary element method from conception to application, *Eng. Analysis with Boundary Elements*, 77: iii-x. <https://doi.org/10.1016/jenganabound.2016.12.001>.
- [28] Xu F., Xie M. & Yue M., 2023. Multigrid Method for Nonlinear Eigenvalue Problems Based on Newton Iteration, *J. Sci. Comput.*, 94, 42 DOI: 10.1007/s10915-022-02070-9.
- [29] Kerboua Y., Lakis A.A., Thomas, M., Marcouiller, L., 2008, Vibration analysis of rectangular plates coupled with fluid, *Applied Mathematical Modelling*, Vol. 32(12): 2570-2586, <https://doi.org/10.1016/j.apm.2007.09.004>.
- [30] Di Lorenzo, E., Manzato, S., Peeters, B., Ruffini, V., Berring, P., Haselbach, P. U., Branner, K., Luczak, M. M. 2020. Modal Analysis of Wind Turbine Blades with Different Test Setup Configurations. *Modal Analysis & Testing*, vol. 8: 143-152. DOI: 10.1007/978-3-030-12684-1_14.
- [31] Lindholm U.S., Kana, D. D., Chu, W.-H., Abramson, H.N., 1965. Elastic Vibration Characteristics of Cantilever Plates in Water, *J Ship Res*, Vol. 9: 11-36, <https://doi.org/10.5957/jsr.1965.9.2.11>.
- [32] Boujleben A., Ibrahimbegovic A., Lefrançois E., 2020. An efficient computational model for fluid-structure interaction in application to large overall motion of wind turbine with flexible blades. *Appl. Math. Model.* Vol. 77: 392–407. <https://doi.org/10.1016/j.apm.2019.07.033>.
- [33] Murawski K., Rózanowski K., Krej M., 2013. Research and Parameter Optimization of the Pattern Recognition Algorithm for the Eye Tracking Infrared Sensor. *Acta Physica Polonica* Vol. A 124: 513-516. <https://doi.org/10.12693/APhysPolA.124.513>.
- [34] Wu W., Sun Q., Luo S., Sun H. 2018. Accurate calculation of aerodynamic coefficients of parafoil airdrop system based on computational fluid dynamic. *International Journal of Advanced Robotic Systems*, vol. 15(2), 172988141876619: 1-16. DOI: 10.1177/1729881418766190.
- [35] Khammas F. A., Hussein Suffer K., Usubamatov R., Mustaffa M. T., 2015. Overview of Vertical Axis Wind Turbine (VAWT) is one of the Wind Energy Application. *In Applied Mechanics and*

Materials Vol. 793: 388–392. Trans Tech Publications, Ltd. <https://doi.org/10.4028/www.scientific.net/AMM.793.388>.

Contribution of Individual Authors to the Creation of a Scientific Article (Ghostwriting Policy)

- Olena Sierikova: conceptualisation, data curation.
- Elena Strelnikova carried out the simulation and the optimization.
- Kyryl Degtyarev: carried out the simulation and the optimization.

Sources of Funding for Research Presented in a Scientific Article or Scientific Article Itself

No funding was received for conducting this study.

Conflict of Interest

The authors have no conflicts of interest to declare.

Creative Commons Attribution License 4.0 (Attribution 4.0 International, CC BY 4.0)

This article is published under the terms of the Creative Commons Attribution License 4.0

https://creativecommons.org/licenses/by/4.0/deed.en_US